Resonant inelastic x-ray scattering in warm-dense Fe compounds beyond the SASE FEL resolution limit

Check for updates

Alessandro Forte [1]✉, Thomas Gawne [2,3], Karim K. Alaa El-Din[1], Oliver S. Humphries [4], Thomas R. Preston [4], Céline Crépisson[1], Thomas Campbell[1], Pontus Svensson [1], Sam Azadi[1], Patrick Heighway[1], Yuanfeng Shi[1], David A. Chin [5], Ethan Smith[5,6], Carsten Baehtz[4], Victorien Bouffetier[4], Hauke Höppner[3], Alexis Amouretti[7,8], David McGonegle[9], Marion Harmand[8], Gilbert W. Collins[5,6,10], Justin S. Wark [1], Danae N. Polsin[5,10] & Sam M. Vinko [1,11]✉

Resonant inelastic x-ray scattering (RIXS) is a widely used spectroscopic technique, providing access to the electronic structure and dynamics of atoms, molecules, and solids. However, RIXS requires a narrow bandwidth x-ray probe to achieve high spectral resolution. The challenges in delivering an energetic monochromated beam from an x-ray free electron laser (XFEL) thus limit its use in few-shot experiments, including for the study of high energy density systems. Here we demonstrate that by correlating the measurements of the self-amplified spontaneous emission (SASE) spectrum of an XFEL with the RIXS signal, using a dynamic kernel deconvolution with a neural surrogate, we can achieve electronic structure resolutions substantially higher than those normally afforded by the bandwidth of the incoming x-ray beam. We further show how this technique allows us to discriminate between the valence structures of Fe and Fe_2O_3, and provides access to temperature measurements as well as M-shell binding energies estimates in warm-dense Fe compounds.

Resonant inelastic x-ray scattering (RIXS) is a powerful spectroscopic tool that has revolutionized the field of material science. It provides detailed information on the electronic, magnetic, and orbital structures of materials with high resolution, thereby offering new opportunities for the exploration of materials and their dynamic processes including electron correlations, charge excitations, spin excitations, and phonon density of states[1,2]. With the advent of x-ray free-electron laser (XFEL) light sources[3], RIXS is also becoming an increasingly appealing technique for the exploration of extreme states of matter[4], including of materials undergoing laser-driven dynamic compression to achieve high pressures[5]. While x-ray diffraction techniques bear witness to a rich collection of exotic physical behaviour exhibited in materials dynamically compressed to high densities[6], the detailed electronic structure and excitation behaviour of such systems remain largely unexplored.

The transient nature of experimentally-realized high energy density (HED) systems necessitates the use of bright x-ray sources with short pulse durations, making XFELs particularly attractive probes. Time-resolved RIXS is appealing in this context as it can provide insight into the time evolution of the electronic structure of such systems, and access a wide range of excitation mechanisms. Traditionally, however, RIXS requires a highly monochromatic x-ray source to yield spectra with satisfactory resolution, which is at odds with the current 0.4% bandwidth of a self-amplified spontaneous emission (SASE) XFEL[7]. SASE bandwidths in the x-ray regime are typically on the order of 20–30 eV, an order of magnitude too large to resolve even basic features in the density of states. Self-seeding techniques can improve the spectral purity of the beam, but the presence of a SASE pedestal remains problematic for high-resolution RIXS measurements[8]. For these reasons, monochromators are typically required, but they come with their own challenges. For one, the signal-to-noise ratio (SNR) is drastically reduced, as most incoming photons are discarded. In addition, the stochastic nature of the FEL generation process also leads to substantial fluctuations in the thermodynamic conditions of the sample, which complicates the data analysis. Importantly, in the study of transient HED systems such

[1]Department of Physics, Clarendon Laboratory, University of Oxford, Oxford, UK. [2]Center for Advanced Systems Understanding (CASUS), Görlitz, Germany. [3]Helmholtz-Zentrum Dresden-Rossendorf (HZDR), Dresden, Germany. [4]European XFEL, Schenefeld, Germany. [5]Laboratory for Laser Energetics, University of Rochester, Rochester, NY, USA. [6]Department of Physics and Astronomy, University of Rochester, Rochester, NY, USA. [7]Graduate School of Engineering, Osaka University, Suita, Japan. [8]Sorbonne Université, Institut de Minéralogie, de Physique des Matériaux et de Cosmochimie, IMPMC, Museum National dH'istoire Naturelle, UMR CNRS 7590, IRD, Paris, France. [9]AWE, Aldermaston, Reading, UK. [10]Department of Mechanical Engineering, University of Rochester, Rochester, NY, USA. [11]Central Laser Facility, STFC Rutherford Appleton Laboratory, Didcot, UK. ✉e-mail: alessandro.forte@physics.ox.ac.uk; sam.vinko@physics.ox.ac.uk

photon losses cannot always be recovered by longer integration times or by higher repetition rates, as the measurement is destructive, and a new system must be created for each new shot. In order to integrate multiple shots to improve overall SNR in such experiments, each shot must contain sufficient signal to be validated independently. This requirement places a fundamental constraint on the signal levels required to field a reliable RIXS diagnostic.

In this work, we present experimental results demonstrating how the electronic structure can be extracted from a RIXS measurement via a deconvolution approach that makes use of the full information contained in the stochastic SASE pulse structure of an XFEL. This idea of correlating the spectroscopic measurements with the photons source spectra has already been used in previous studies[9,10]. The resolution achieved with our approach is limited only by the resolution of the spectrometer measuring the emitted RIXS signature, and by the SNR, but not by the overall bandwidth or structure of the probe beam itself. Using a SASE pulse with bandwidth of ~ 19 eV we show we can extract the density of states of Fe and Fe_2O_3 with resolutions of 6-9 eV. This is sufficient to observe pre-edge features in Fe_2O_3, demonstrate material specificity, and to extract the temperature of the system heated by the x-ray pulse. Our results illustrate how this correlation approach can robustly deconvolve the polychromatic signal, making the SASE spectrum of an XFEL an exploitable feature rather than an inconvenience requiring mitigation by a monochromator. Importantly, this implies that developments in XFEL technology that increase the energy of the XFEL pulse, rather than its spectral brightness at the expense of photon number, can provide a promising alternative for accessing improved, higher resolution spectroscopic data.

Results

The RIXS cross-section for scattering into a solid angle $d\Omega$ can be written as[11,12]:

$$\frac{d^2\sigma}{d\Omega d\omega_2} \propto \sum_f \left| \sum_n \frac{\langle f|\mathcal{D}'^\dagger|n\rangle \langle n|\mathcal{D}|i\rangle}{E_n - \hbar\omega_1 - E_i + i\Gamma_n} \right|^2 \times \delta(E_f - E_i + \hbar\omega_2 - \hbar\omega_1), \tag{1}$$

where E_i, E_n and E_f are the energies of the initial, intermediate and final states of the system, $\mathcal{D}$ is the transition operator[11], and Γ_n is the lifetime of the intermediate state. The incident and outgoing photons have energies $\hbar\omega_1$ and $\hbar\omega_2$ respectively. The RIXS process is shown schematically in Fig. 1. Following the work of Humphries et al.[4], we focus on the exploration of the broad structure of unoccupied valence states, rather than low-energy excitations, thus seeking to extract the density of states from the RIXS measurement. In this case, Eq. (1) can be simplified and written explicitly in terms of the density of states ρ, the matrix element for transitions between initial and intermediate states M, and the Kα line intensity A_f as

$$\frac{d^2\sigma}{d\Omega d\omega_2} = \hbar\left(\frac{e}{mc}\right)^4 \frac{\omega_2}{\omega_1} \sum_f A_f[1 - f_{FD}(\hbar\omega_1 - \hbar\omega_2 + \epsilon_{L,f}; T)]$$
$$\times \rho(\hbar\omega_1 - \hbar\omega_2 + \epsilon_{L,f})\frac{|M(\hbar\omega_1 - \hbar\omega_2 + \epsilon_{L,f})|^2}{(\hbar\omega_2 - (\epsilon_{L,f} - \epsilon_K))^2 + \Gamma_f^2}, \tag{2}$$

where f_{FD} denotes the Fermi-Dirac occupation function, precluding transitions to occupied states. The energy $\epsilon_{L,f}$ denotes the binding energy of the (L-shell) electron that decays to fill the (K-shell) core hole, whose binding energy is denoted by ϵ_K. The derivation of this result can be found in the supplementary materials of ref. 4. We will use this expression as a starting point to interpret the experimental results.

RIXS as dynamic kernel deconvolution

The intensity of the RIXS spectrum as a function of the scattered photon energy $\hbar\omega_2$, can be found by integrating the differential cross-section over all incident photon energies $\hbar\omega_1$, and over the solid

angle detected for each outgoing energy $\Omega(\omega_2)$:

$$I(\omega_2) = \Omega(\omega_2)\int_{-\infty}^{+\infty}\hbar d\omega_1\,\Phi(\omega_1)\partial_{\omega_2}\sigma, \tag{3}$$

with $\partial_{\omega_2}\sigma$ given by Eq. (2), $\Phi(\omega_1)$ representing the incoming SASE spectrum and $\Omega(\omega_2)$ calculable from the geometry of the experimental setup. The expression above takes the form of a sum of convolutions with a dynamic kernel $\Phi(\omega_1)$. The kernel is dynamic because it represents the SASE pulse, which is formed of a series of narrow spikes in photon energy that change stochastically from shot to shot. If we assume a typical dataset will contain N single shots indexed by k, with associated RIXS spectra $I_k(\omega_2)$, each will be given by Eq. (3) using the corresponding XFEL spectra $\Phi_k(\omega_1)$.

The cross-section contains information on the vacant part of the DOS via the sum in Eq. (2), including a modulation due to the energy-dependent transition matrix elements $M(\varepsilon)$. We denote this experimentally accessible quantity as the effective density of states, ρ_{eff}, given by

$$\rho_{eff}(\varepsilon) = [1 - f_{FD}(\varepsilon; T)]\rho(\varepsilon)|M(\varepsilon)|^2. \tag{4}$$

We note that this quantity is effectively the x-ray absorption spectrum of the material, but without the disadvantage of any blurring due to the x-ray source bandwidth[13], and with the advantage of having being obtained in just a single shot, therefore avoiding the risk of being deformed by thermodynamic fluctuations in the sample due to edge-crossing. With the notation given in (4) we can describe the RIXS measurement formally as an operator P_{RIXS} that links the k measured spectra I_k to the effective DOS and the spectral FEL kernel Φ_k:

$$I_k(\omega_2) = P_{RIXS}[\Phi_k, \rho_{eff}](\omega_2). \tag{5}$$

The effective DOS can be found by inverting P_{RIXS} with respect to ρ_{eff}:

$$\rho_{eff}(\varepsilon) = P_{RIXS}^{-1}[I_k, \Phi_k](\varepsilon), \tag{6}$$

which is valid for each k.

The RIXS cross-section is relatively small, and single-shot measurements typically have low SNR. This makes the use of standard inversion methods via deconvolution, such as the Richardson-Lucy method[14], unsuitable for single-shot analysis. Integrating over many shots ($I_k \to \bar{I}$ and $\Phi_k \to \bar{\Phi}$) can mitigate such limitations in SNR, but it also limits the resolution with which we can extract ρ_{eff}. Alternatively, a machine learning approach could be used to construct an estimator to approximate P_{RIXS}^{-1} from a large labelled dataset of known pairings (ρ_{eff}, I_k, Φ_k)[15]. However, given the stochastic nature of the FEL pulse profile and the complexity of the RIXS operator, collecting and validating a sufficiently large dataset of this kind can be a considerable challenge in its own right, in addition to the high complexity required for such an inversion estimator. The lack of a robust approach to process low SNR data represents a considerable bottleneck for x-ray spectroscopy in high energy density physics applications[10].

Rather than searching for a general estimator to approximate the highly complex object P_{RIXS}^{-1}, we instead look for a suitable approximation $\tilde{\rho}_{eff}$ to the much simpler function ρ_{eff}. The adopted procedure is illustrated in Fig. 2. We use the known forward model P_{RIXS} to calculate the predicted spectral intensity given a known Φ_k and the estimate $\tilde{\rho}_{eff}$:

$$\tilde{I}_k(\omega_2) = P_{RIXS}[\Phi_k, \tilde{\rho}_{eff}](\omega_2). \tag{7}$$

Considering that, for our cases with low photon rates, the uncertainties of the single shots are approximately constant over ω_2, the spectral intensity $\tilde{I}_k$ is then used to compute an L_2 loss function

$$\mathcal{L}_k = ||\tilde{I}_k(\omega_2) - I_k(\omega_2)||_2, \tag{8}$$

which provides a measure of the quality of the approximate $\tilde{\rho}_{\text{eff}}$ given the observed $I_k(\omega_2)$. Improving the approximation for $\tilde{\rho}_{\text{eff}}$ can now be viewed as a standard machine learning optimization problem. We represent $\tilde{\rho}_{\text{eff}}$ using a trainable feed-forward neural network acting as a universal approximator, and implement P_{RIXS} in automatically differentiable form[16]. This allows us to use backpropagation and gradient descent to systematically improve $\tilde{\rho}_{\text{eff}}$ by minimizing the objective loss $\mathcal{L}$. We explicitly use the known physics, given by Eq. (3), to provide the inductive bias for extracting the desired electronic structure from the spectroscopic measurement.

The energy resolution with which $\tilde{\rho}_{\text{eff}}$ can be found is given by the SNR of the single RIXS spectra and the energy resolutions with which I_k and Φ_k are measured. While the method can, in principle, be used to optimize single shot data, we instead perform batching of the data to improve the SNR across multiple shots (see the subsection 'Details of the machine learning approach' in Methods for more information). In contrast to standard averaging approaches, the resolution is not degraded by such a merging of multiple shots, since each pairing (I_k, Φ_k) is still considered individually in the optimization process.

Synthetic data

As a first validation of the method, we attempt to reconstruct synthetic DOS data using our deconvolution approach. We choose a spiky DOS, which is both challenging to tackle for traditional deconvolution algorithms, but which is also indicative of narrow bound states, $d-$ band features, and resonances. The DOS data is fed into the forward model of Eq. (5), alongside
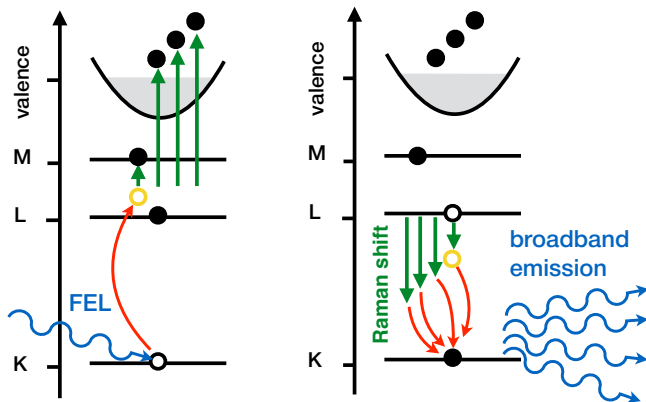
Fig. 1 | Schematic of the RIXS process for our cases of interest. This is composed of an energy non-conserving absorption, which excites a K-shell electron (left), followed by an energy non-conserving emission produced by the decay of a L-shell electron into the K-shell core hole (right). The overall process conserves energy. The accessible states are the vacant states in the valence band or, for finite temperature systems, in thermally ionized bound states.

a series of realistic SASE spectra, to produce a synthetic RIXS intensity profiles. We add three levels of Gaussian noise to these spectra, with standard deviations being respectively 0%, 15% and 30% of the RIXS spectra maxima. Some typical resulting spectra are shown in Fig. 3a–c. Note that at the highest level of noise, the features in the spectrum are barely recognizable.

These synthetic spectra are provided to our deconvolution scheme, alongside the corresponding SASE spectra. We show the resulting extracted DOS in Fig. 3d–f. Our approach shows good convergence of the extracted DOS for all levels of noise up to 30%. However, the accuracy of reconstruction decreases as we raise the level of noise, with the extracted ρ_{eff} starting to miss small or narrow features, especially for large detuning energies. This behaviour is expected, since the area under a DOS feature and its detuning, i.e., its distance from resonance, are the two main parameters that determine the intensity of the feature in the RIXS spectrum. Bright features closer in energy to the resonance are thus more robust to low SNR. Another common factor that deteriorates the accuracy of the reconstructions is the presence of spurious oscillations in the extracted ρ_{eff}. These oscillations are a typical byproduct of deconvolution, and are present on energy-scales smaller than the kernel's bandwidth. Regardless, the successful extraction of features using our approach even from spectra dominated by noise, as shown in Fig. 3c, remains significant.

A note is in order: we denote as RIXS scattering processes with detuning energies up to 150 eV, following the notation adopted in[4], however, other names (e.g., high energy resolution off-resonance spectroscopy) have also been used to describe such scattering processes in the literature[17,18]. Unlike in ref. 4 where the incident photon energies are varied, in this work we fix the XFEL central energy approximately 50 eV below the iron K edge to optimize the extraction of the valence density of states.

To demonstrate the efficacy of our method, in Fig. 4 we show the quality of the ρ_{eff} reconstruction as a function of the number of shots in the dataset for four different approaches and two noise levels. The blue and red curves employ the paradigm described in Fig. 2 to reconstruct ρ_{eff}: with blue circles we show the results using all individual experimental pairs (I_k, Φ_k), while the results using average values $(\bar{I}, \bar{\Phi})$ are shown with red squares. Similarly to what has been done in[9,10], we also directly invert Eq. (5) via standard numerical techniques for comparison (see subsection 'Details of the numerical approach' in Methods), both for the individual pairs (diamond markers) and for the averaged spectra (triangle markers). We find that while the direct inversion method achieves the best results in the absence of noise, its performance degrades rapidly as noise is added. This is due to the characteristics of P_{RIXS}, which maps very different ρ_{eff} into similar RIXS spectra (contraction map), making its inversion an ill-conditioned problem. On the other hand, our approach shows little variation on the quality of the reconstructed DOS with noise, and is thus more robust. In particular, we observe that with our method the results obtained for a 15% noise level converge to those achieved without noise already for a relatively restrained N ≈ 50. The comparison between single shot and averaged

Fig. 2 | Representation of the scheme used to extract physical information on the electronic structure of a material from a SASE-based RIXS measurement. The estimate of ρ_{eff}, represented by a feedforward neural network, is fed to the RIXS differentiable model alongside the measured XFEL spectrum. The model outputs the calculated RIXS spectrum, which is then compared with the experimental spectrum. This comparison generates a loss function used to adjust the neural network parameters, thereby refining the ρ_{eff} estimate. The resolution of the resulting density of states depends on the resolutions of the spectrometers used to measure the RIXS signal and the profile of the SASE pulse, but is independent of the SASE pulse structure or bandwidth.
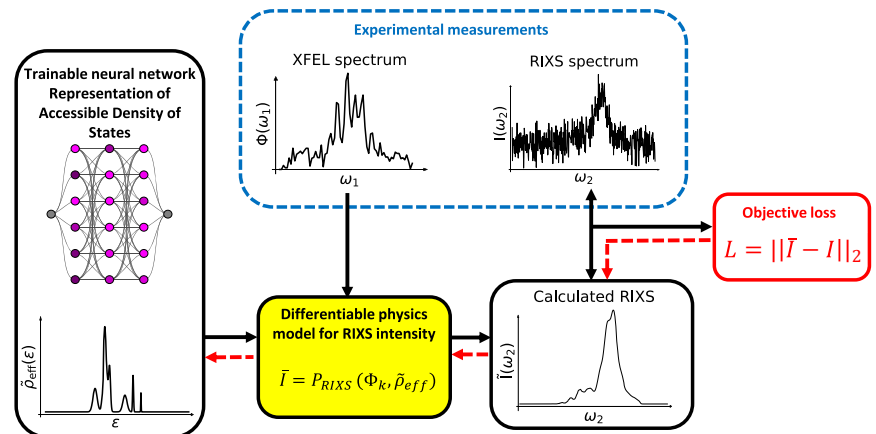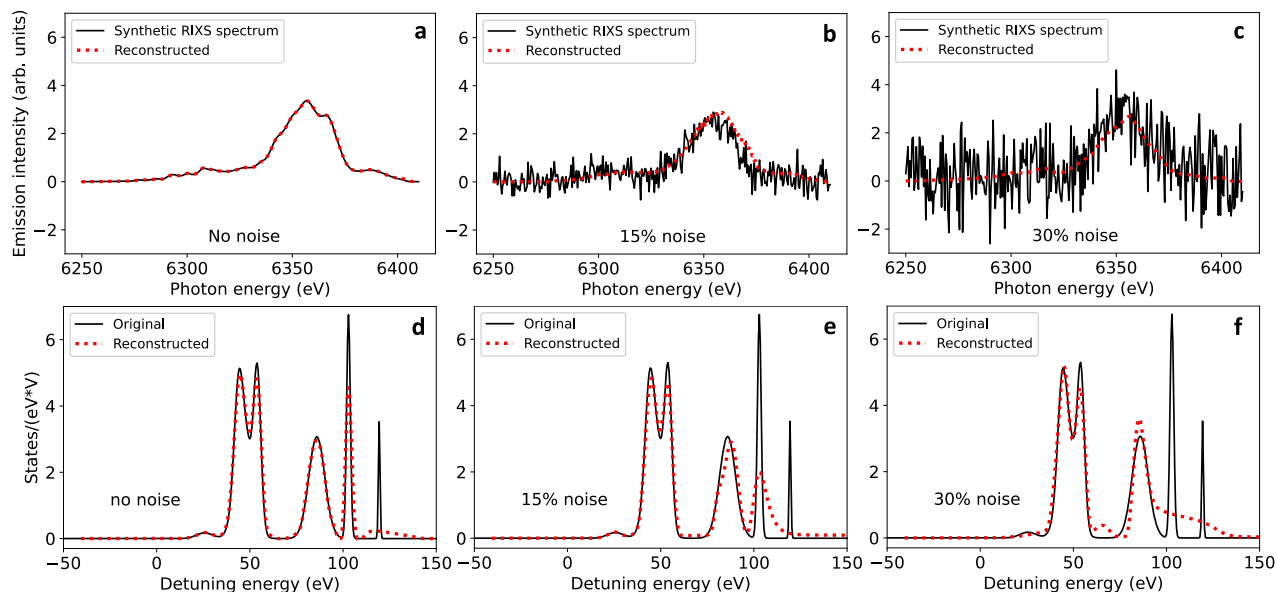
Fig. 3 | Reconstruction of a synthetic density of states from a RIXS spectrum at varying levels of noise, using a realistic SASE XFEL profile. A total of 50 single shots were used. We show examples of the synthetic RIXS spectra in **a**–**c**, with the corresponding reconstructions in **d**–**f**. The technique is robust to noise, owing to the strong inductive bias given by the model, and the stochastic nature of the SASE pulse profile Φ that allows us to oversample the DOS. The zero of the DOS energies is centred at the resonance.
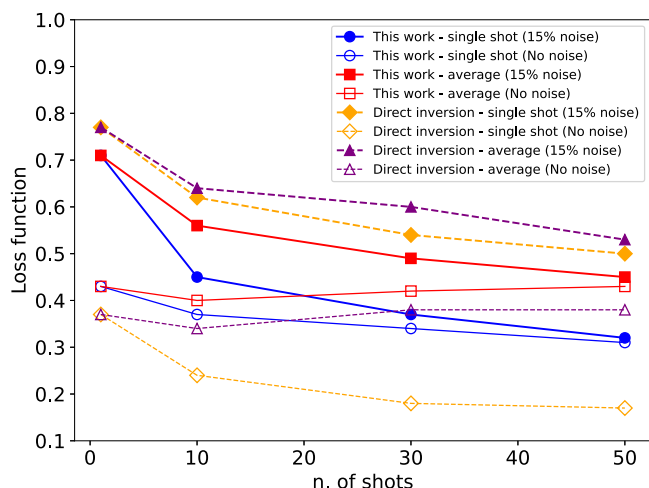

Fig. 4 | Reconstruction quality of the RIXS spectrum as a function of the number of shots N included in the inversion dataset. The DOS used is that shown in Fig. 3a. While the direct inversion works best for noiseless data, the quality rapidly deteriorates for real data with noise. In contrast, our approach is fairly insensitive to noise. The loss function employed for this plot is a weighted L_2 distance between the reconstructed and the original DOS, with bigger weights for the energy regions where features are present. This is achieved defining the weighted L_2 norm as $1/F \sum_i |d\rho_{\mathrm{eff}}/d\epsilon|(\epsilon_i)(\tilde{\rho}_{\mathrm{eff}}(\epsilon_i) - \rho_{\mathrm{eff}}(\epsilon_i))^2$, where ρ_{eff} is the original DOS and F is a normalization factor.

analysis indicates that averaged calculations suffice for broad features, but that shot-by-shot analysis is required to capture finer structure, and that the averaging process leads to a loss in resolution. This can be explained considering that deconvolution is more efficient with spiky XFEL spectra, characteristic of the single shot case, rather than with relatively broad Gaussian XFEL spectra, which occur in averaged calculations. Specifically, in the absence of noise, where no gain on the SNR is obtained through averaging, the use of the averaged spectra deteriorates the quality of the reconstructions as N grows.

Experimental data

We now turn to the analysis of experimental RIXS spectra, which have been obtained at the HED instrument of the European XFEL[19]. The measurement was performed using x-rays at a photon energy of 7060 eV, focused to spot sizes of 7–10 μm onto samples of Fe and Fe_2O_3. The total pulse energy in the beam ranged between 500 and 1000 μJ, but it was constrained to be between 700 and 800 μJ for the analysed data in order to limit the sample thermodynamic variations. The focal spot size was optimized in-situ to maximize x-ray heating, diagnosed via the observed emission from the Fe M-shell. The targets consisted of 20 μm thick freestanding Fe foils, and 15 μm thick Fe_2O_3, deposited on 50 μm of plastic. These thicknesses correspond to a single absorption length or below at the photon energies used, and they were chosen to maintain a uniform temperature from x-ray heating. The FEL was operated in SASE mode[20], with an average pulse duration of 40 fs and a spectral bandwidth of around 19 eV full-width-half-maximum (FWHM). The photon energy was tuned to lie just below the Fe K-edge to ensure that RIXS was the dominant scattering process. By ensuring that the bandwidth of the pulse is sufficiently close to the Kβ transition energy (1s-3p) we further ensure that the ionization of the 3p state can be measured. The 3p state is fully occupied in the ground state, and is only depopulated in the experiment due to the heating of the electrons via the intense x-ray irradiation. The RIXS signal was measured using a cylindrically bent Highly Annealed Pyrolytic Graphite (HAPG) spectrometer in the von Hamos configuration[21], coupled to a Jungfrau detector. The experimentally determined resolution of the spectrometer and setup, including crystal resolution, pixel size effects and source size, was 5.5 eV. The spectrum of the SASE beam was determined on a shot-to-shot basis via a Si beamline spectrometer with resolution of 0.3 eV[22].

Examples of single-shot experimental spectra are shown in Fig. 5, alongside with the corresponding extracted electronic structure. We see that the typical level of noise for a single-shot RIXS spectrum is on the order of 15%, comparable to the cases examined for the synthetic data. The experimental reconstructions of ρ_{eff} are compared with density functional theory calculations (see section 'Theoretical calculations' in Methods), which allow us to identify various features in the experimental data, and to evaluate the resolution with which $\rho_{\mathrm{eff}}(\epsilon)$ can be extracted in practice, given
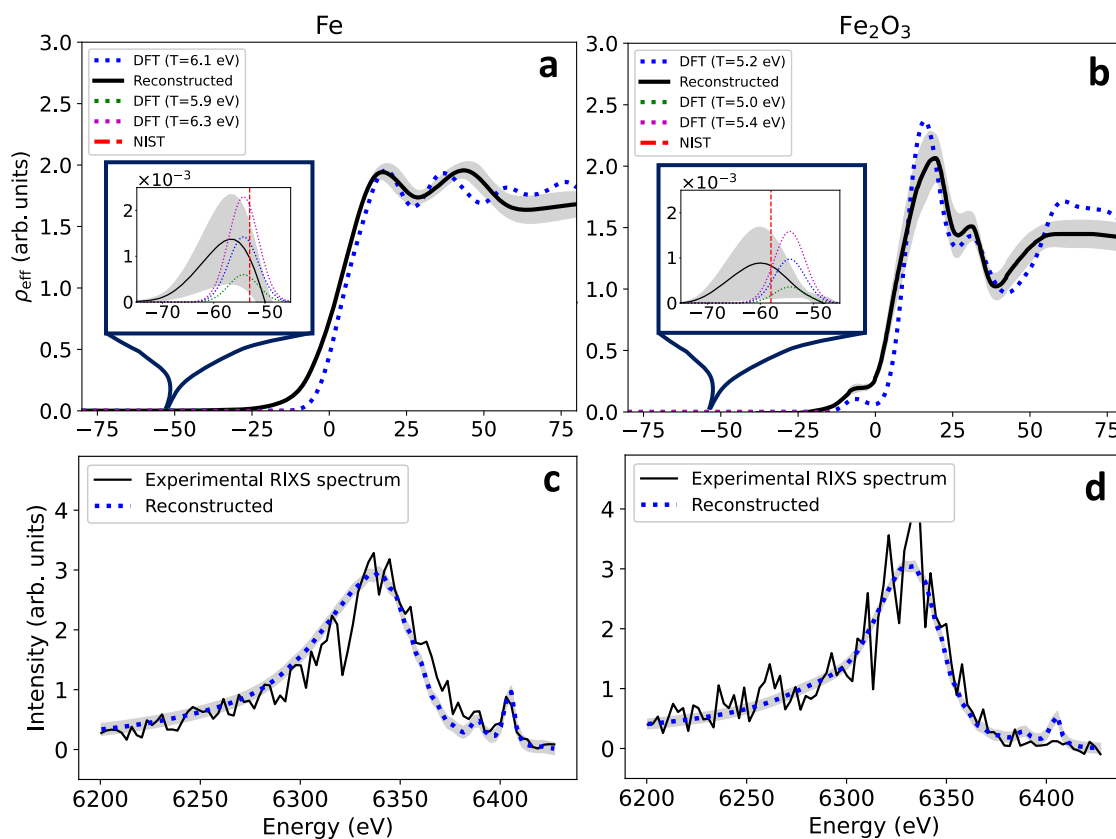
Fig. 5 | Measured accessible density of states of Fe and Fe_2O_3 a, b, reconstructed from the RIXS measurements, along with their respective experimental spectra c, d. The grey bands indicate the standard deviation. The measured data are compared with theoretical DFT calculations, for which we used a smearing width of 7 eV for Fe_2O_3 and 9 eV for Fe[47]. The insets show the reconstruction of the M-shell vacant states, located around -55 eV. This feature is only present if the M-shell is thermally ionized by the x-ray beam, thus allowing us to estimate the temperature of the sample. The red dashed vertical line indicates a reference M-shell binding energy, taken from[27].

our experimental setup. The experimental ρ_{eff} have been reconstructed using our dynamic kernel deconvolution scheme over approximately 18,000 RIXS shots for each material. We conducted 6 independent fitting processes, for both materials, with different random seeds for the NN. The average and standard deviation of the resulting outputs have been taken, respectively, as the best estimate for ρ_{eff} and its error. The error on the experimental RIXS spectra due to noise, which is propagated through to ρ_{eff}, becomes negligible because of the large amount of experimental shots. Hence, the error is due only to the stochasticity of the NN optimization.

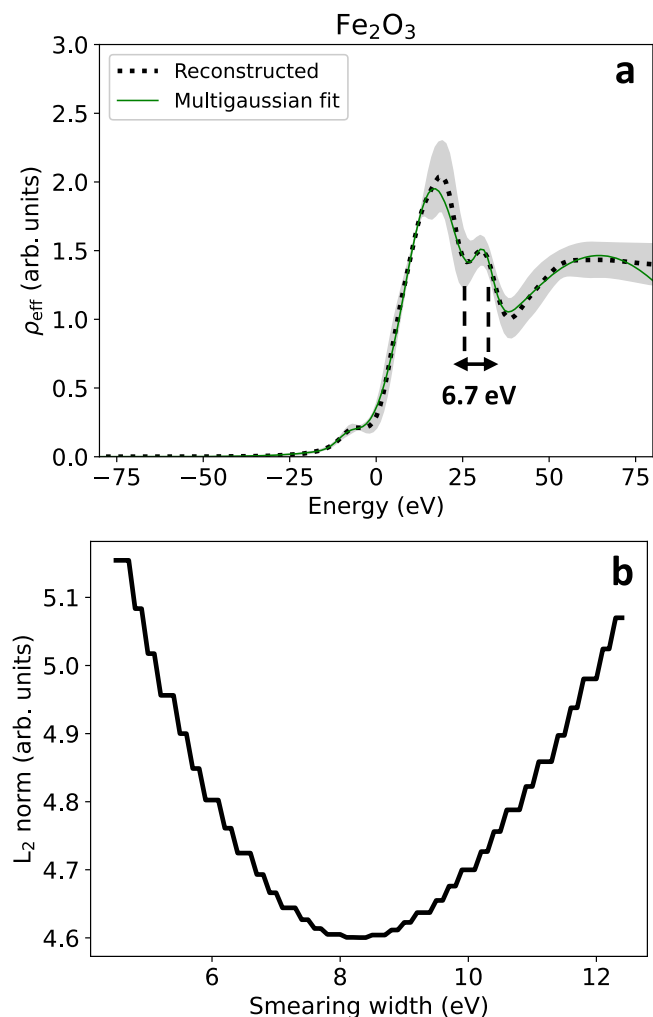### Estimation of the resolution

The experimental reconstructions in Fig. 5 agree well with the theoretical predictions, and we note that we are able to extract densities of states with a fairly complex structure from RIXS spectra with relatively low SNR. We estimated the resolution of the extracted ρ_{eff} with two different methods, shown in Fig. 6. In panel (a) we fit the reconstructed Fe_2O_3 ρ_{eff} with a superposition of multiple Gaussians. This fitting is then used to achieve an estimate of the narrowest feature width we reconstruct, and therefore, of the resolution. This width is found to be 6.7 eV. Another method to evaluate the resolution is to consider the L_2 distance between the experimental ρ_{eff} and the DFT predictions, as a function of the smearing width applied to the latter. This curve is plotted in Fig. 6b. The minimum of this curve can be found for a smearing width around 8.2 eV, yielding another estimate for the resolution of our extracted ρ_{eff}. The small discrepancy between the two methods can be traced back to the different resolutions with which different parts of the DOS seem to be reconstructed (e.g., the continuum slope and the small valence band peak). This resolution is somewhat lower than the limit of 5.5 eV imposed by the spectrometer resolution in our experimental setup.

We attribute this small difference primarily to the SNR of the experimental data, which was fairly low, as the data collection was done in single-shot mode (see Fig. 5). Nevertheless, the reconstructed electronic structures show resolutions up to three times higher than the spectral FWHM of the XFEL pulse. We show in Fig. 5a, b that this allows us to distinguish the environment in which an Fe atom is embedded, via differences in the electronic structure of Fe in the insulating Fe_2O_3 or in the metallic state. Such a distinction cannot be made via RIXS with the normal spectral resolution of the SASE beam of ~20 eV, as it is illustrated in Fig. 7.

Characteristic of the measured electronic structures

The comparison of the electronic structure with the orbital-projected DOS reveals that the pre-edge feature in Fe_2O_3, located around -10 eV, contains a mixture of the 2p oxygen states and the 3d iron states, which are indistinguishable at these resolutions. The band gap between these states and the conduction ones, predicted by experimental measurements[23,24] to have a width of approximately 2 eV, is visible in the reconstruction as a slightly convex plateau located at just below 0 eV.

In addition to the modulation in the continuum and the pre-edge feature in the Fe_2O_3 case, we are able to reconstruct the M-shell for both materials, as shown in the insets of Fig. 5a–b. Despite the small area of these features due to the low thermal de-occupation, they are amplified in the RIXS spectra by their vicinity to the resonant energies. Thus, the reconstructed ρ_{eff} gives us a method to experimentally estimate the binding energy (BE) of the M-shell in extreme thermodynamic conditions–a quantity difficult to obtain via theoretical approaches[25,26]. The values found from the reconstructions are (-56 ± 3) eV for Fe and (-59 ± 5) eV for Fe_2O_3. As we observed that finite-temperature effects like pressure ionization have a

Fig. 6 | Two different approaches for the estimate of the extracted DOS resolution. In panel (**a**) this is carried out by fitting a superposition of multiple Gaussians to the reconstructed DOS, whereas in panel (**b**) we consider the L_2 distance between the experimental reconstruction and the DFT simulations as a function of their smearing width. The error intervals on the reconstructed DOS in panel (**a**) are identical to those of Fig. 5.

negligible impact on BE for the temperatures reached in the experiment, we compared our estimates with the M-shell binding energies documented in the NIST database[27] and we found our results to be compatible with these reference values.

Similarly to what has been done in[4], we can exploit the M-shell feature to estimate the sample temperature averaged over the beam pulse duration. However, contrary to[4], where the sample temperature is found by fitting the theoretical RIXS spectra to the experimental ones, here we can directly fit the DFT-computed density of accessible states ($\rho|M|^2$) to the reconstructed $\tilde{\rho}_{\text{eff}}$:

$$[1 - f_{FD}(\epsilon; T)]\rho_{\text{DFT}}(\epsilon)|M_{\text{DFT}}(\epsilon)|^2 \overset{!}{=} \tilde{\rho}_{\text{eff}}(\epsilon), \tag{9}$$

where the chemical potential must be computed self-consistently. This new procedure enables us to reduce the error bars on the temperatures estimates compared to the previous work, yielding temperatures of (6.1 ± 0.2) eV for Fe and of (5.2 ± 0.2) eV for Fe_2O_3. We note that these estimates justify the implicit assumption that depopulation of the M-shell is given mainly by thermal collisions (and not by photoionization), and therefore can be described by the factor $(1 - f_{FD})$. As observed in ref. 28, these extracted

temperatures provide a good estimate of the peak temperature reached in the target during the irradiation.

Conclusions

We have used a neural surrogate and differentiable programming to establish a machine learning routine that can extract hyper-resolved DOS measurements from RIXS diagnostics at XFEL experiments through large amounts of data. This procedure could represent an alternative way forward in XFEL experiments which prioritizes the increase of the laser pulse energy over the development of monochromation techniques. Our method for the extraction has been compared to other approaches, demonstrating its robustness to noise present in the experimental measurements. We have furthermore shown that the analysis of RIXS spectra through this method can be used to gain a plethora of useful information, from distinguishing between different material spectra to inferring temperatures in HED regimes. A potential future step to further improve the resolution would envisage the inclusion of the setup instrument function in the forward model. This is particularly beneficial in instances where we can model the effects of specific setup components, such as the broadening due to a mosaic crystal[29]. Beyond the application to RIXS analysis for further materials and experiments, this machine learning approach can provide a promising avenue for other diagnostics, such as X-Ray Thomson Scattering (XRTS) or the extraction of structure factors from diffraction data. Even though each such application requires a differentiable programming implementation of the corresponding forward model, the combination of machine learning with known physical inductive biases under this scheme constitutes a powerful tool for the analysis of experimental data and the estimation of physical quantities that can only be measured indirectly.

Methods

The physical parameters of P_{RIXS}, chosen for our synthetic and experimental data analysis, are specific to iron and have been taken from[30]. We report them in Table 1.

Details of the machine learning approach

The estimator used to reconstruct $\rho_{\text{eff}}(\varepsilon)$ was a feed-forward neural network with a single input and output, 4 hidden layers with 40 nodes each, and the *softplus* activation function[31]. The neural network was trained by means of the ADAM[32] optimizer with the initial learning rate set to 10^{-3}. This optimization, together with the automatic differentiation of the forward model, was carried out using the library PyTorch[33]. To ensure a good performance of this scheme, we have identified the necessity of addressing the vanishing gradient problem[34] by omitting exponentially small factors in the gradient backpropagation. The training was performed splitting the set of experimental spectra (I_k, Φ_k for $k = 0, 1, \ldots, N$) into batches, whose size was increased dynamically during the training to shift from exploratory to exploitative training. The optimization routine considers the loss function, and the respective gradients, on an entire batch to update model parameters at each step. Furthermore, the training has been carried out over many epochs, i.e., rolling over all the N shots multiple times. Finally, during the training we constrained the output of the neural network $\tilde{\rho}_{\text{eff}}(\varepsilon)$ to be positive, a fundamental physical requirement.

Details of the numerical approach

To extract ρ_{eff} from a set of RIXS and SASE spectra without making use of machine learning techniques, we employ the following routine:

1. We first discretize the RIXS operator for each FEL spectrum Φ_k, computing the associated matrices M_k for $k = 1, 2, \ldots, N$. Each M_k is constructed taking as its i-th column $P_{\text{RIXS}}[\Phi_k, \rho_i]$, where $(\rho_i)_j = \delta_{i,j}$, with $i, j = 1, 2, \ldots, L$ and L the length of ρ_{eff}. Note that this discretization is possible because P_{RIXS} is a linear operator in ρ_{eff}.
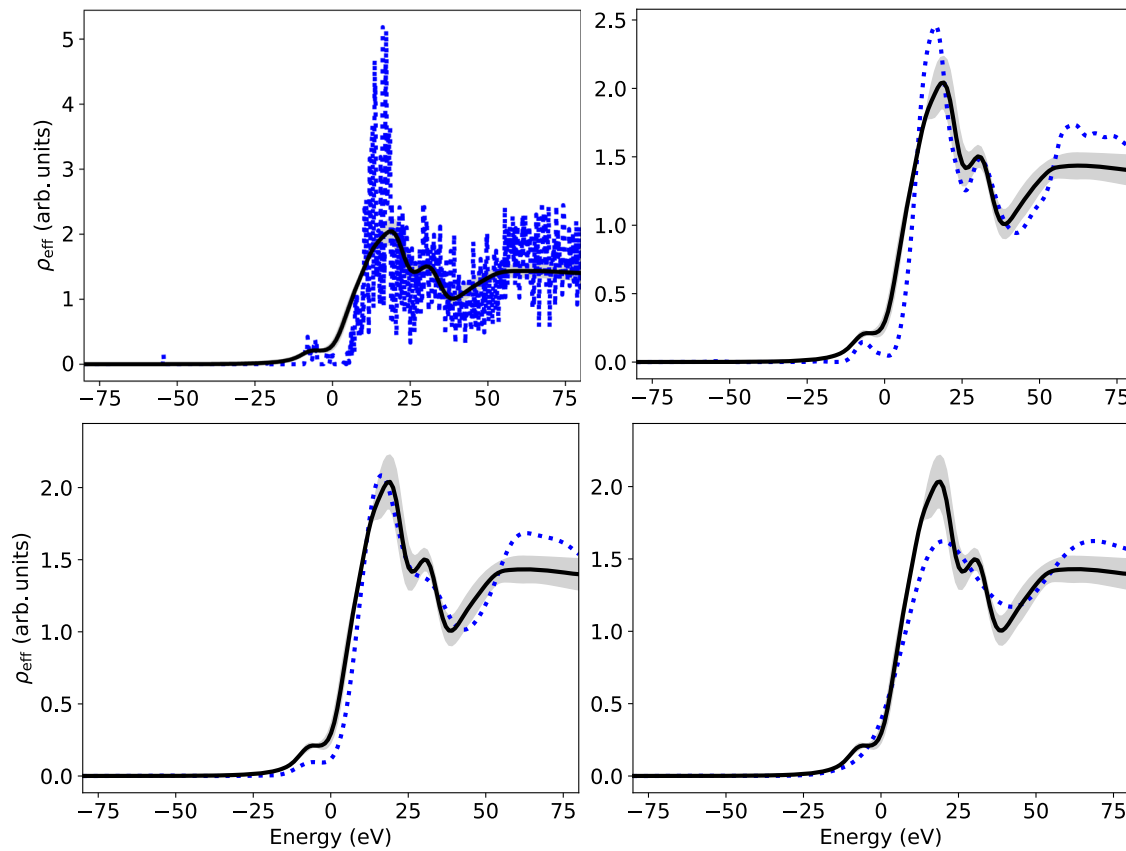
Fig. 7 | Comparison between the reconstructed ρ_{eff} for Fe_2O_3 (solid black lines) and the DFT simulations (dashed blue lines) with smearing widths of 0.2, 5, 10, and 20 eV respectively. It is observable that with a smearing of 20 eV, as it would be given by the SASE bandwidth, the characteristic features of Fe_2O_3 are no longer visible.

2. We then construct the macro-linear system of equations in ρ_{eff} by stacking the matrices M_k and the RIXS spectra I_k as:

$$\begin{bmatrix} M_1 \\ M_2 \\ \vdots \\ M_N \end{bmatrix} \rho_{\text{eff}} := M\rho_{\text{eff}} = \begin{bmatrix} I_1 \\ I_2 \\ \vdots \\ I_N \end{bmatrix} := I \qquad (10)$$

Notice that the matrix M is in general not square.

3. Finally, we approximate the solution of this linear system, and hence ρ_{eff} using the conjugate gradient descent method[35].

This idea of discretizing the physical process operator and inverting the associated matrix has already been employed in the field of spectroscopic analysis[10]. When working with the averaged spectra, we just search for a

Table 1 | Physical parameters used in this work

Parameter[units]	f	Value
ϵ_K [eV]	1, 2	-7112
$\epsilon_{L,f}$ [eV]	1	-723
	2	-708.5
A_f	1	50
	2	100
Γ_f [eV]	1	3
	2	2.55

Iron has two L-shell states, implying two possible final states $f = 1, 2$.

solution of the linear system $\bar{M}\rho_{\text{eff}} = \bar{I}$, where $\bar{M}$ is constructed using the averaged FEL spectrum $\bar{\Phi}$.

Theoretical calculations

We simulated the electronic structure of Fe and Fe_2O_3 using finite-temperature density functional theory (DFT) with a locally-modified version of the ABINIT v8.10.3 code[36–38]. The relevant modification is the inclusion of the hybrid Kohn-Sham plane-wave-approximation scheme[39] as described by ref. [40] to enable accurate high temperature calculations. The ABINIT code is used to solve the Kohn-Sham (KS) system[41], which provides the KS states and eigenvalues. The DOS is given by the latter, while the former can be used to calculate the dipole transition matrix elements from the Fe 1s core state to the calculated valence states[42]. The orbital-projected DOS was also calculated to aid in identifying features in the total DOS.

The ion cores were represented using the projector-augmented wave (PAW) scheme[43], with Fe and O PAW potentials generated using the *Atompaw* code[44]. For efficiency, the Fe 1s, 2s, 2p orbitals and the O 1s orbital were treated with the frozen-core approximation. This approximation is suitable for the relatively low temperatures (< 10 eV) reached in this experiment, as these orbitals are not thermally ionized.

Calculations were performed at electron temperatures of 300 K, 1 eV, 5 eV, and 10 eV, with the ions frozen in their ambient crystal lattice positions. This further approximation is justified by the femtosecond duration of the XFEL pulses, during which all the spectral emission of interest occurs. This timescale is substantially shorter than the electron-phonon coupling times of several picoseconds. The Fe calculations were therefore performed in a bcc primitive unit cell containing a single atom. Simulations were carried out with 120 bands, a $30 \times 30 \times 30$ k-point grid, with a cut-off energy of 50 Ha for the PAW pseudo-wavefunctions and 150 Ha for the all-electron wavefunctions. The Fe_2O_3 calculations were performed in its α-phase[45], with a unit cell containing 30 atoms, 1440 bands, a $6 \times 6 \times 1$ k-point grid (the

latter direction being the long direction of the unit cell), with a cut-off energy of 20 Ha for the PAW pseudo-wavefunctions and 100 Ha for the all-electron wavefunctions.

For the exchange-correlation functional, the PBE form of the generalized gradient approximation (GGA) was used for both the Fe and O atoms. We used the corrective approach of a Hubbard potential (DFT $+U$) to recover the band gap in Fe_2O_3, with a value of $U = 4.0$ eV for the Fe $l = 2$ channel to be able to recover a band gap of ~ 2.0 eV, as given by[46]. As the higher temperatures we consider here are substantial compared with the value of U, we choose $U = 4.0$ eV for all Fe_2O_3 calculations. Small adjustments to the value of U at a temperature of 5 eV did not show meaningful changes to the electronic structure, justifying this approach.

Reporting summary

Further information on research design is available in the Nature Portfolio Reporting Summary linked to this article.

Data availability

The data that support the findings of this work are available from the corresponding author upon reasonable request.

Code availability

The code used for this study is available from the corresponding author upon reasonable request.

References

1. Ament, L. J. P., van Veenendaal, M., Devereaux, T. P., Hill, J. P. & van den Brink, J. Resonant inelastic x-ray scattering studies of elementary excitations. *Rev. Mod. Phys.* **83**, 705–767 (2011).
2. Jia, C., Wohlfeld, K., Wang, Y., Moritz, B. & Devereaux, T. P. Using rixs to uncover elementary charge and spin excitations. *Phys. Rev. X* **6**, 021020 (2016).
3. Huang, Z. & Kim, K.-J. Review of x-ray free-electron laser theory. *Phys. Rev. Special Top.-Accel. Beams* **10**, 034801 (2007).
4. Humphries, O. S. et al. Probing the electronic structure of warm dense nickel via resonant inelastic x-ray scattering. *Phys. Rev. Lett.* **125**, 195001 (2020).
5. Hicks, D. et al. Laser-driven single shock compression of fluid deuterium from 45 to 220 gpa. *Phys. Rev. B* **79**, 014112 (2009).
6. Kohara, S. et al. Structural studies of disordered materials using high-energy x-ray diffraction from ambient to extreme conditions. *J. Phys. Condens. Matter* **19**, 506101 (2007).
7. Zhu, D. et al. A single-shot transmissive spectrometer for hard x-ray free electron lasers. *Appl. Phys. Lett.* **101** (2012).
8. Liu, S. et al. Cascaded hard x-ray self-seeded free-electron laser at megahertz repetition rate. *Nat. Photon.* 1–8 (2023).
9. Fuller, F. D. et al. Resonant x-ray emission spectroscopy from broadband stochastic pulses at an x-ray free electron laser. *Commun. Chem.* **4**, 84 (2021).
10. Kayser, Y. et al. Core-level nonlinear spectroscopy triggered by stochastic x-ray pulses. *Nat. Commun.* **10**, 4761 (2019).
11. Kramers, H. A. & Heisenberg, W. Über die streuung von strahlung durch atome. *Zeitschr. Phys. A Hadrons Nuclei* **31**, 681–708 (1925).
12. Kotani, A. & Shin, S. Resonant inelastic x-ray scattering spectra for electrons in solids. *Rev. Mod. Phys.* **73**, 203 (2001).
13. Henderson, G. S., De Groot, F. M. & Moulton, B. J. X-ray absorption near-edge structure (xanes) spectroscopy. *Rev. Mineral. Geochem.* **78**, 75–138 (2014).
14. Fish, D., Brinicombe, A., Pike, E. & Walker, J. Blind deconvolution by means of the richardson–lucy algorithm. *JOSA A* **12**, 58–65 (1995).
15. Stielow, T. & Scheel, S. Reconstruction of nanoscale particles from single-shot wide-angle free-electron-laser diffraction patterns with physics-informed neural networks. *Phys. Rev. E* **103**, 053312 (2021).
16. Schoenholz, S. & Cubuk, E. D. JAX MD: a framework for differentiable physics. *Adv. Neural Inf. Process. Syst.* **33**, 11428–11441 (2020).
17. Błachucki, W. et al. High energy resolution off-resonant spectroscopy for x-ray absorption spectra free of self-absorption effects. *Phys. Rev. Lett.* **112**, 173003 (2014).
18. Szlachetko, J. et al. Communication: The electronic structure of matter probed with a single femtosecond hard x-ray pulse. *Struct. Dyn.* **1** (2014).
19. Zastrau, U. et al. Conceptual design report: Dynamic laser compression experiments at the hed instrument of european xfel. Tech. Rep., European X-Ray Free-Electron Laser Facility GmbH (2017).
20. Geloni, G. et al. Coherence properties of the european xfel. *N. J. Phys.* **12**, 035021 (2010).
21. Preston, T. et al. Design and performance characterisation of the hapg von hámos spectrometer at the high energy density instrument of the european xfel. *J. Instrum.* **15**, P11033 (2020).
22. Kujala, N. et al. Hard x-ray single-shot spectrometer at the european x-ray free-electron laser. *Rev. Sci. Instrum.* **91** (2020).
23. Mohanty, S. & Ghose, J. Studies on some α-fe2o3 photoelectrodes. *J. Phys. Chem. Solids* **53**, 81–91 (1992).
24. Westre, T. E. et al. A multiplet analysis of fe k-edge 1s→ 3d pre-edge features of iron complexes. *J. Am. Chem. Soc.* **119**, 6297–6314 (1997).
25. Stewart, J. C. & Pyatt Jr, K. D. Lowering of ionization potentials in plasmas. *Astrophys. J.* **144**, 1203 (1966).
26. Ecker, G. & Kröll, W. Lowering of the ionization energy for a plasma in thermodynamic equilibrium. *Phys. Fluids* **6**, 62–69 (1963).
27. Lemmon, E. W., Huber, M. L., McLinden, M. O. et al. Nist standard reference database 23. *Reference fluid thermodynamic and transport properties (REFPROP)* **9** (2010).
28. Humphries, O. et al. Probing the electronic structure of warm dense nickel via resonant inelastic x-ray scattering. *Phys. Rev. Lett.* **125**, 195001 (2020).
29. Schlesiger, C., Anklamm, L., Malzer, W., Gnewkow, R. & Kanngießer, B. A new model for the description of x-ray diffraction from mosaic crystals for ray-tracing calculations. *J. Appl. Crystallogr.* **50**, 1490–1497 (2017).
30. Henke, B., Lee, P., Tanaka, T., Shimabukuro, R. & Fujikawa, B. Low-energy x-ray interaction coefficients: photoabsorption, scattering, and reflection: E= 100–2000 ev z= 1–94. *At. Data Nuclear Data Tables* **27**, 1–144 (1982).
31. Zheng, H., Yang, Z., Liu, W., Liang, J. & Li, Y. Improving deep neural networks using softplus units. In *2015 International joint conference on neural networks (IJCNN)*, 1–4 (IEEE, 2015).
32. Kingma, D. P. & Ba, J. L. Adam: A Method for Stochastic Optimization. *3rd International Conference on Learning Representations, ICLR 2015 - Conference Track Proceedings* (2014). https://arxiv.org/abs/1412.6980v9.
33. Ketkar, N., Moolayil, J., Ketkar, N. & Moolayil, J. Introduction to pytorch. *Deep Learning with Python: Learn Best Practices of Deep Learning Models with PyTorch* 27–91 (2021).
34. Hochreiter, S. The vanishing gradient problem during learning recurrent neural nets and problem solutions. *Int. J. Uncertainty Fuzz. Knowledge-Based Syst.* **6**, 107–116 (1998).
35. Luenberger, D. G., Ye, Y. et al. *Linear and nonlinear programming*, vol. 2 (Springer, 1984).
36. Gonze, X. et al. Recent developments in the ABINIT software package. *Comput. Phys. Commun.* **205**, 106–131 (2016).
37. Torrent, M., Jollet, F., Bottin, F., Zérah, G. & Gonze, X. Implementation of the projector augmented-wave method in the ABINIT code: application to the study of iron under pressure. *Comput. Mater. Sci.* **42**, 337–351 (2008).

38. Bottin, F., Leroux, S., Knyazev, A. & Zérah, G. Large-scale ab initio calculations based on three levels of parallelization. *Comput. Mater. Sci.* **42**, 329–336 (2008).

39. Zhang, S., Wang, H., Kang, W., Zhang, P. & He, X. T. Extended application of Kohn-Sham first-principles molecular dynamics method with plane wave approximation at high energy—From cold materials to hot dense plasmas. *Phys. Plasmas* **23**, 042707 (2016).

40. Blanchet, A., Clérouin, J., Torrent, M. & Soubiran, F. Extended first-principles molecular dynamics model for high temperature simulations in the Abinit code: Application to warm dense aluminum. *Comput. Phys. Commun.* **271**, 108215 (2022).

41. Kohn, W. & Sham, L. J. Self-consistent equations including exchange and correlation effects. *Phys. Rev.* **140**, A1133–A1138 (1965).

42. Mazevet, S., Torrent, M., Recoules, V. & Jollet, F. Calculations of the transport properties within the paw formalism. *High Energy Density Phys.* **6**, 84–88 (2010).

43. Blöchl, P. E. Projector augmented-wave method. *Phys. Rev. B* **50**, 17953–17979 (1994).

44. Holzwarth, N., Tackett, A. & Matthews, G. A Projector Augmented Wave (PAW) code for electronic structure calculations, Part I: atompaw for generating atom-centered functions. *Comput. Phys. Commun.* **135**, 329–347 (2001).

45. Sakurai, S., Namai, A., Hashimoto, K. & Ohkoshi, S.-i First observation of phase transformation of all four fe2o3 phases ($\gamma \rightarrow \varepsilon \rightarrow \beta \rightarrow \alpha$-phase). *J. Am. Chem. Soc.* **131**, 18299–18303 (2009).

46. Xia, C., Jia, Y., Tao, M. & Zhang, Q. Tuning the band gap of hematite α-fe2o3 by sulfur doping. *Phys. Lett. A* **377**, 1943–1947 (2013).

47. Parr, R. G. & Yang, W. Density-functional theory of the electronic structure of molecules. *Ann. Rev. Phys. Chem.* **46**, 701–728 (1995).

Author contributions
S.M.V., J.S.W., A.F., M.H., G.W.C., D.M., O.S.H., T.R.P., C.B., and T.G. conceived and designed the experiment. M.H., A.A., D.N.P., and D.A.C. manufactured the samples employed for the study. A.F., S.M.V., T.G., O.S.H., T.R.P., C.B., C.C., T.C., P.S., S.A., P.H., Y.S., D.A.C., E.S., and D.N.P. carried out the experiment and the real-time data analysis. V.B. and H.H. contributed to the beamline control. A.F., S.M.V., and K.K.A. developed the deconvolution approach. A.F. conducted the studies on the synthetic data with contributions from K.K.A. A.F. performed the post-experiment data analysis with help from T.G., D.N.P., and S.A. T.G. performed the DFT simulations. A.F., T.G, K.K.A., and S.M.V. wrote the manuscript with contributions from all authors.

Competing interests
The authors declare no competing interests.

Additional information
Supplementary information The online version contains supplementary material available at https://doi.org/10.1038/s42005-024-01752-0.

Correspondence and requests for materials should be addressed to Alessandro Forte or Sam M. Vinko.

Peer review information *Communications Physics* thanks the anonymous reviewers for their contribution to the peer review of this work. A peer review file is available.

Reprints and permissions information is available at http://www.nature.com/reprints

Publisher's note Springer Nature remains neutral with regard to jurisdictional claims in published maps and institutional affiliations.